PHOTONICS Research

Controllable photonic spin Hall effect with phase function construction

Yanliang He,[1,†] Zhiqiang Xie,[1,†] Bo Yang,[1,†] Xueyu Chen,[1] Junmin Liu,[2] Huapeng Ye,[3] Xinxing Zhou,[4] Ying Li,[1] Shuqing Chen,[1,*] and Dianyuan Fan[1]

[1]International Collaborative Laboratory of 2D Materials for Optoelectronics Science and Technology, and Engineering Technology Research Center for 2D Material Information Function Devices and Systems of Guangdong Province, Institute of Microscale Optoelectronics, Shenzhen University, Shenzhen 518060, China
[2]College of New Materials and New Energies, Shenzhen Technology University, Shenzhen 518118, China
[3]Guangdong Provincial Key Laboratory of Optical Information Materials and Technology & Institute of Electronic Paper Displays, South China Academy of Advanced Optoelectronics, South China Normal University, Guangzhou 510006, China
[4]Synergetic Innovation Center for Quantum Effects and Applications, School of Physics and Electronics, Hunan Normal University, Changsha 410081, China
*Corresponding author: shuqingchen@szu.edu.cn

Received 21 January 2020; revised 26 March 2020; accepted 6 April 2020; posted 6 April 2020 (Doc. ID 388838); published 28 May 2020

Photonic spin Hall effect (SHE) provides new opportunities for achieving spin-based photonics applications. However, flexibly manipulating the spin-dependent splitting (SDS) of photonic SHE and imposing extra phase modulation on the two spin components are always a challenge. Here, a controllable SHE mechanism based on phase function construction is reported. It is concluded that the phases with specific functional structures performing a coordinate translation are equivalent to integrating a gradient phase to the original phases. Hence, the original phase can be used for independent phase modulation, and the gradient phase originating from the coordinate translation is capable of manipulating the SDS. A metasurface with Pancharatnam–Berry phase that can impose conjugate phases to the two spin components of light is fabricated to verify this mechanism. By shifting the light position, the SDS is continuously manipulated in the visible region, which is successfully used for detecting the polarization ellipticity. The extra phase modulation is also performed with the original phase and thus enables measuring singular beams. It is anticipated that the controllable SHE manipulation method may open new avenues in the fields of spin photonics, optical sensing, optical communications, etc.

https://doi.org/10.1364/PRJ.388838

1. INTRODUCTION

Photonic spin Hall effect (SHE), originating from the spin-orbit interaction and manifesting as spin-dependent splitting (SDS) [1–3], has attracted extensive attention in recent years. Based on SHE, a large variety of applications in the fields of optical analog computing [4,5], weak measurement [6–8], optical sensing [9], etc. have been developed. Generally, the spin-orbit interaction attributes to two types of geometric phase: the Rytov–Vladimirskii–Berry (RVB) phase (related to the direction of wave vector) and the Pancharatnam–Berry (P-B) phase (associated with the light polarization) [2,8,10–14]. For the RVB phase, the SDS occurs in the real position space when linearly polarized light beam reflects or refracts at a planar interface. When the light beam passes through an inhomogeneous anisotropic medium, the SDS in the momentum space arises from the P-B phase. According to light propagation direction, the SHE can also be classified as reflection [1,6,7,11] and transmission type [15–19]. The SDS originating from the RVB phase is usually less than a wavelength due to the weak spin-orbit interaction. However, the SDS originating from the P-B phase increases with the propagation distance, which is much larger than the RVB's. Based on the sensitive relationship between the SDS and interface, many weak measurement techniques were proposed to measure the physical parameters of nanostructures, such as metallic films and graphene [6,7]. Moreover, the polarization ellipticity and handedness of light can also be characterized by using the giant SDS from the P-B phase [20].

To achieve more diverse applications, such as the optical computing of spatial differentiation realized via analyzing the orthogonal polarization states of light and the differential effect obtained through tuning the SDS [5], the controllable photonic SHE is highly demanded to flexibly manipulate the spin-polarized photons. Except for manipulating the SDS, extra phase modulation is also pursued for performing more operations on the spin components. To manipulate the SDS in the

transverse and longitudinal directions simultaneously, the gradient phase combined with a conventional lens was used [21]. Moreover, the helical phase was integrated with the gradient phase to impose orbital angular momenta to the two spin components [22].

Flexible manipulation of the photonic SHE is always a challenge in practical applications. In the RVB-based tunable SDS, varying the thickness of the reflecting layered structure is the most commonly used method [7]. The graphene and graphene-like materials were employed to avoid changing the device structure, where the SDS could be dynamically tuned by varying the Fermi energy [23]. Unfortunately, limited by the naturally tiny SDS, the tuning range, which is usually on the order of a wavelength, is quite low. Hence, the SDS coming from the P-B phase with large manipulation ranges seems to be more attractive. By tailoring the space-variant P-B phase contributed by cylindrical vector beams (CVBs), the photonic SHE can also be tuned; however, it involves changing the structure of incident light beams, which is very difficult in practical applications [24]. Meanwhile, these conventional SHE manipulation methods make it hard to meet the requirement of system integration and extra phase modulation.

Metasurfaces, which enable engineering the spatial phases of light by defining the geometry, orientation, and arrangement of subwavelength-scale building blocks [25–27] and exhibit excellent ability in manipulating the spin-orbit interaction, have been widely used to produce SDS [28–35]. To realize the extra phase modulation of the two spin components, the metasurface can be integrated with other functional phases [21,22]. However, once the structure is fabricated, the P-B phase in the metasurface is fixed. To achieve tunable SDS, the metasurfaces combined with phase change and elastic materials are potential candidates because the states of these materials are thermally and mechanically controllable [36–38]. The chalcogenide phase change material composed of alloys of germanium, antimony, and tellurium can transit between the disordered-amorphous state and ordered-crystalline state with temperature control, which is used for manipulating the "ON" and "OFF" states of metasurfaces [38]. The states of ultrathin metasurfaces fabricated on the elastic substrate are also tunable, and the tuning range depends on the stretch of materials [37]. However, the regulation range and continuous adjustability of these methods are limited by the finite response states of materials. Moreover, the working wavelength of the metasurface is also limited by the response wavelength of materials, and the bandwidth is hard to improve. One of the most enticing promises that delimit the further development of controllable SHE might come from a new manipulating mechanism without involving tunable materials.

In this work, we propose a controllable SHE based on phase function construction in which the phases (such as twisting phase and lens phases) with specific functional structures performing a coordinate translation are equivalent to integrating a gradient phase to the original phases, which can be used to realize controllable SDS in the momentum space. Meanwhile, with the original phases, the extra phase modulation of the two orthogonal spin components can be achieved simultaneously. To verify this mechanism, we fabricate a dielectric geometric P-B phase metasurface by writing spatially variant grooves in the silica glass to impose conjugate twisting phases to the two spin components. It is experimentally demonstrated that the SDS can be continuously manipulated in the visible region (three wavelengths of 633, 532, and 475 nm with the diffraction efficiencies of 98.72%, 95.05%, and 90.06% are chosen) by shifting the incident light beams. With the giant SDS, the polarization ellipticity is successfully measured. Moreover, the extra phase modulation is achieved under the action of twisting phase, with the result that the spin components of singular beams are separated and diffracted into specific intensity patterns. It is also demonstrated that P-B phase metasurface succeeds in detecting the topological charges and polarization orders of arbitrary singular beams [the vortex beams (VBs) with the topological charges of 1 and 2, the CVBs with the polarization orders of −1 and 2, and the cylindrical vector vortex beams (CVVBs) with the topological charges and polarization orders of (1, 2) and (2, −1)]. These results confirm that the controllable SHE based on phase function construction can be used for manipulating the SDS and extra phase modulation, which may pave new avenues in spin-photonics applications.

2. THEORY AND PRINCIPLE

We consider a light beam paraxially propagating along axis z, and the phase-correcting metasurface, located in the transverse (x, y) plane, whose action is the spin-dependent modulation of the incident beam phase. If the incident beam with the transverse amplitude distribution $f(x,y)$ crosses such a P-B phase metasurface, the beam's complex amplitude transforms as $f(x,y)\exp[i\sigma_{\pm}\phi(x,y)]$, where $\phi(x,y) = 2\varphi(x,y)$ and $\varphi(x,y)$ is the local optical axis direction of the metasurface, $\sigma_{+} = +1$ for the left (LCP) and $\sigma_{-} = -1$ for the right (RCP) circularly polarized beams, respectively. The spin-dependent phase gradient is one of the conventional methods to achieve SDS. For example, the SDS in the horizontal (x) direction can be realized if the function $\phi(x,y)$ contains the summand bx with a certain constant parameter b:

$$a(x^2 - y^2) + bx = a\left(x^2 + \frac{b}{a}x - y^2\right) = a\left[\left(x + \frac{b}{2a}\right)^2 - y^2\right] - \frac{b^2}{4a}, \tag{1}$$

$$a(x^2 + y^2) + bx = a\left(x^2 + \frac{b}{a}x + y^2\right) = a\left[\left(x + \frac{b}{2a}\right)^2 + y^2\right] - \frac{b^2}{4a}, \tag{2}$$

$$axy + bx = ax\left(y + \frac{b}{a}\right). \tag{3}$$

The elementary deduction [Eqs. (1)–(3)] shows that in cases when $\phi(x,y) = a(x^2 + y^2)$, or $\phi(x,y) = a(x^2 - y^2)$, or $\phi(x,y) = axy$, the phase-gradient transformation can be realized via shifting the incident beam with respect to the center of the phase-correcting plate (e.g., in the horizontal direction; see Fig. 1). In the practical applications, the P-B phase metasurface

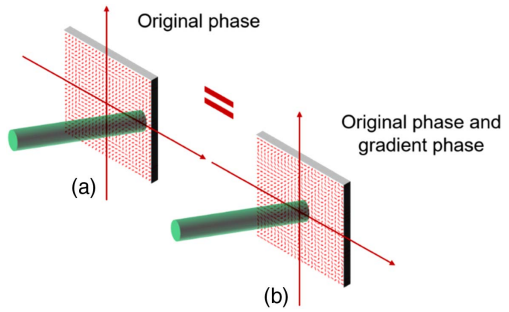

Fig. 1. Shifting the (a) incident position onto the P-B phase metasurface carrying the original phases is equivalent to (b) centrally incident on the P-B phase metasurface carrying the original phase and gradient phase.

can be realized by designing the optical axes profiles. The Jones matrix of the metasurface under half-wave phase retardance can be written as

$$J = \begin{bmatrix} \cos(2\varphi) & \sin(2\varphi) \\ \sin(2\varphi) & -\cos(2\varphi) \end{bmatrix}. \tag{4}$$

With an LCP or RCP Gaussian beam incident, the output field can be expressed as

$$\begin{aligned} J_1 &= E_1 \begin{bmatrix} \cos(2\varphi) & \sin(2\varphi) \\ \sin(2\varphi) & -\cos(2\varphi) \end{bmatrix} \begin{bmatrix} 1 \\ i \end{bmatrix} \\ &= E_1 \begin{bmatrix} \cos(2\varphi) + i\sin(2\varphi) \\ \sin(2\varphi) - i\cos(2\varphi) \end{bmatrix} \\ &= E_1 \exp(i2\varphi) \begin{bmatrix} 1 \\ -i \end{bmatrix} = E_1 \exp(i\phi) \begin{bmatrix} 1 \\ -i \end{bmatrix}, \end{aligned} \tag{5}$$

$$\begin{aligned} J_2 &= E_2 \begin{bmatrix} \cos(2\varphi) & \sin(2\varphi) \\ \sin(2\varphi) & -\cos(2\varphi) \end{bmatrix} \begin{bmatrix} 1 \\ -i \end{bmatrix} \\ &= E_2 \begin{bmatrix} \cos(2\varphi) - i\sin(2\varphi) \\ \sin(2\varphi) + i\cos(2\varphi) \end{bmatrix} \\ &= E_2 \exp(-i2\varphi) \begin{bmatrix} 1 \\ i \end{bmatrix} = E_2 \exp(-i\phi) \begin{bmatrix} 1 \\ i \end{bmatrix}, \end{aligned} \tag{6}$$

where E_1 and E_2 are the simplified amplitude of LCP and RCP Gaussian beams. Hence, by properly designing the optical axis of metasurface under half-wave retardance, the above functions can be performed with P-B phase devices.

After that, we find that there are two typical phases that can meet the above functional structure. They are the twisting phase [39] and the dynamical phase lens [21], whose phase functions can be expressed as

$$\phi_1 = u(x\cos\theta - y\sin\theta)(x\sin\theta + y\cos\theta), \tag{7}$$

$$\phi_2 = \frac{\pi}{\lambda}\left(\frac{x^2 + y^2}{f}\right). \tag{8}$$

In the twisting phase ϕ_1, u is the certain constant strength factor, and θ is the azimuthal angle. When $\theta = 45°$, Eq. (7) satisfies the case $a(x^2 - y^2)$, and $\theta = 0°$ satisfies the case axy. In the lens phase ϕ_2, λ is the wavelength, and f is the focal length. Figure 2 summarizes the phase introduced by P-B phase metasurface carrying the twisting phase, or gradient phase, or dynamical phase lens, or the combination phases under the illumination of LCP and RCP light. The first row presents the optical axis profiles forming the twisting phase, gradient phase, lens phase, and the combination phases. The phases imparted to the LCP and RCP light beams are shown in the second and third rows. From the optical axes and phase patterns, we can see that the twisting phase or lens phase added together with the gradient phase is equivalent to making a coordinate

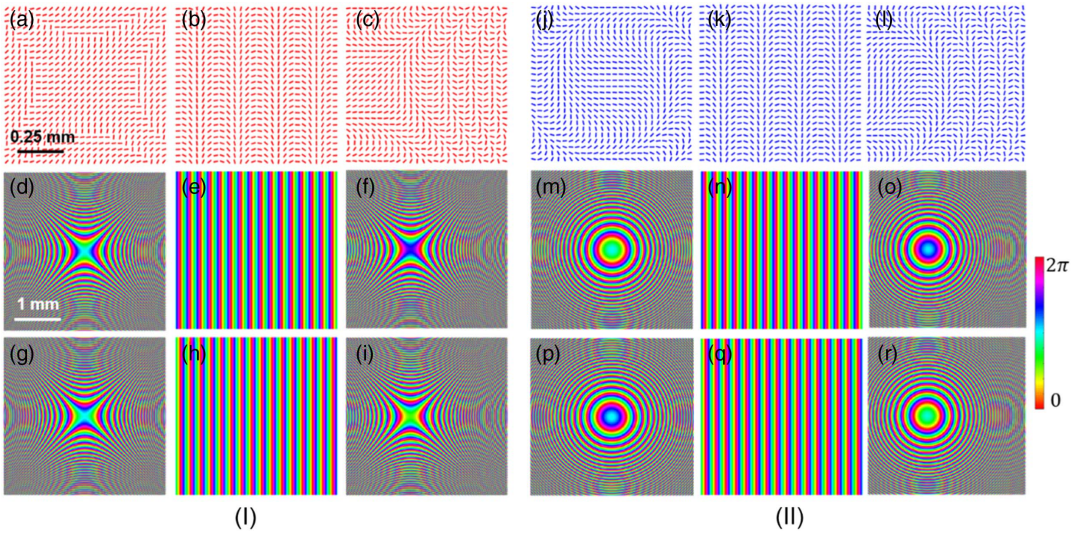

Fig. 2. (I) Illustration of the twisting phase adding together with the gradient phase. (a)–(c) Two-dimensional slow-axis orientation patterns of the twisting phase, gradient phase, and combination phase. (d)–(i) Phases introduced to the LCP and RCP light. (II) Illustration of the lens phase adding together with the gradient phase. (j)–(l) Two-dimensional slow-axis orientation patterns of the lens phase, gradient phase, and combination phase. (m)–(r) Phases introduced to the LCP and RCP light.

translation of the original phases, which agrees well with the theoretical analysis.

Hence, the P-B phase metasurfaces engineered with the twisting phase or lens phase can dynamically manipulate the SDS by shifting the incident beam with respect to the center of the metasurface.

Assuming that the linearly polarized Gaussian beam illuminates the metasurface carrying the twisting phase ($\theta = 45°$) with a lateral shift of Δd, Eq. (7) can be written as

$$\frac{u}{2}(x+\Delta d)^2 - \frac{u}{2}y^2 = \frac{u}{2}x^2 + u(\Delta d)x + \frac{u}{2}(\Delta d)^2 - \frac{u}{2}y^2. \quad (9)$$

As depicted in Eq. (9), a gradient phase [$\psi = u(\Delta d)x$] is produced. Furthermore, referring to Ref. [32], we analyze the relationship between the incident position shift (Δd) and the two separated spin components' interval (ρ):

$$\rho = 2\left(\frac{\Delta k_x}{k_0}\right)z, \qquad \Delta k_x = 2\frac{\partial \psi}{\partial x}\vec{e}_x, \quad (10)$$

$$\rho = 4\left(\frac{u(\Delta d)}{k_0}\right)z, \quad (11)$$

where k_x is the x component of the wave vector, $\vec{e}_x$ is the x directional unit vector, $k_0 = 2\pi/\lambda$ is the wavenumber, and z is the transmission distance. Thus, we can adjust the interval between the two spin components via shifting the incident beams, and even the structure of the metasurface is fixed. The locations of the two spin components can be swapped by reversing the sign of the lateral shift.

The extra phase modulation can be performed with the action of the twisting phase or the dynamic phase lens. According to previous work [39], the VB, which is modulated with a twisting phase that diffracts into a specific intensity pattern, can be used for topological charge recognition. Thus, we can manipulate the SDS by varying the position shift of incident light, and the topological charge recognition can be achieved with the modulation of twisting phases.

3. RESULTS AND ANALYSIS

A. Tunable SDS in the Geometric P-B Phase Metasurface

1. Relationship between SDS and Position Shift

To experimentally verify the proposed mechanism, we have fabricated a geometric P-B phase metasurface by writing spatially variant nanogrooves in the fused silica glass substrate, which can vary the optical axes distribution and impose conjugate twisting phases to the LCP and RCP light. The induced nanogrooves can modulate the refractive indices to form birefringence in the isotropic glass sample [40]. The directions of the local optical axes (fast and slow axes) are perpendicular and parallel to the grooves, respectively. The fabrication processing is given in detail in Appendix A. The schematic diagram of the SDS with a linearly polarized Gaussian beam illuminating the metasurface is shown in Fig. 3(a). By selecting a proper incident position shift, the LCP and RCP components of the output beam are separated. Meanwhile, affected by the twisting phase, the Gaussian beam intensity is evolved into fringes. Because the twisting phases acting on the LCP and RCP components are opposite, there is a relative rotation between the diffraction patterns of the two components. The photograph in Fig. 3(b) shows that the nanostructure is fabricated inside the glass slab. Figure 3(c) presents the polariscopic imaging result carried out with two crossed linear polarizers.

In the experiment, the metasurface is illuminated with a linearly polarized Gaussian beam, which is generated by a He-Ne laser (Thorlabs HNL210L-FC; the working wavelength, 633 nm; the maximum output power, 21 mW). The output beam is transversely split into LCP and RCP components by the metasurface, which is illustrated in the measured Stokes parameters S_3 at the transmission distance of 500 mm, as shown in Fig. 4(a). The detection method of S_3 refers to Ref. [41]. From the S_3 parameters, we can see that the interval between the two spin components increases with the incident position shift (Δd), and the locations of the LCP and RCP components are swapped with the contrary incident position

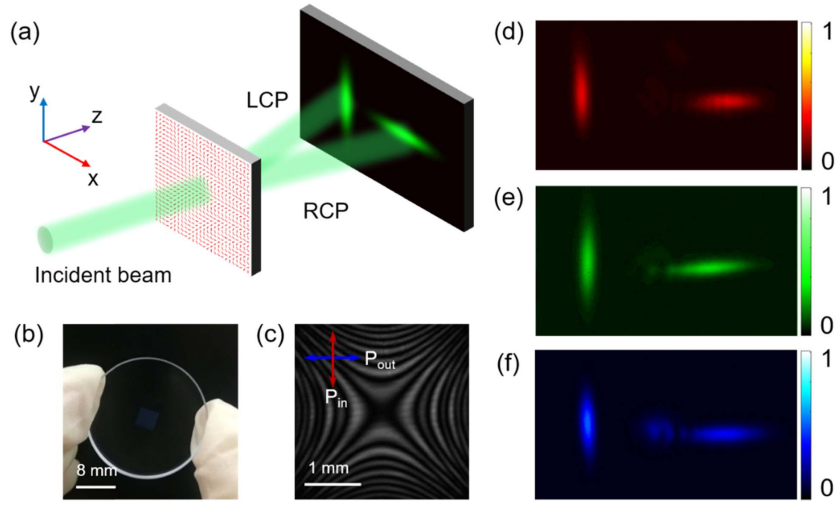

Fig. 3. (a) Illustration of the Gaussian beam illuminating the dielectric P-B phase metasurface. (b) Captured picture of the fabricated metasurface. (c) Polariscopic analysis carried out by optical polarization imaging. (d)–(f) Measured SDS intensity (normalized) images of Gaussian beams at different wavelengths (633, 532, and 475 nm).

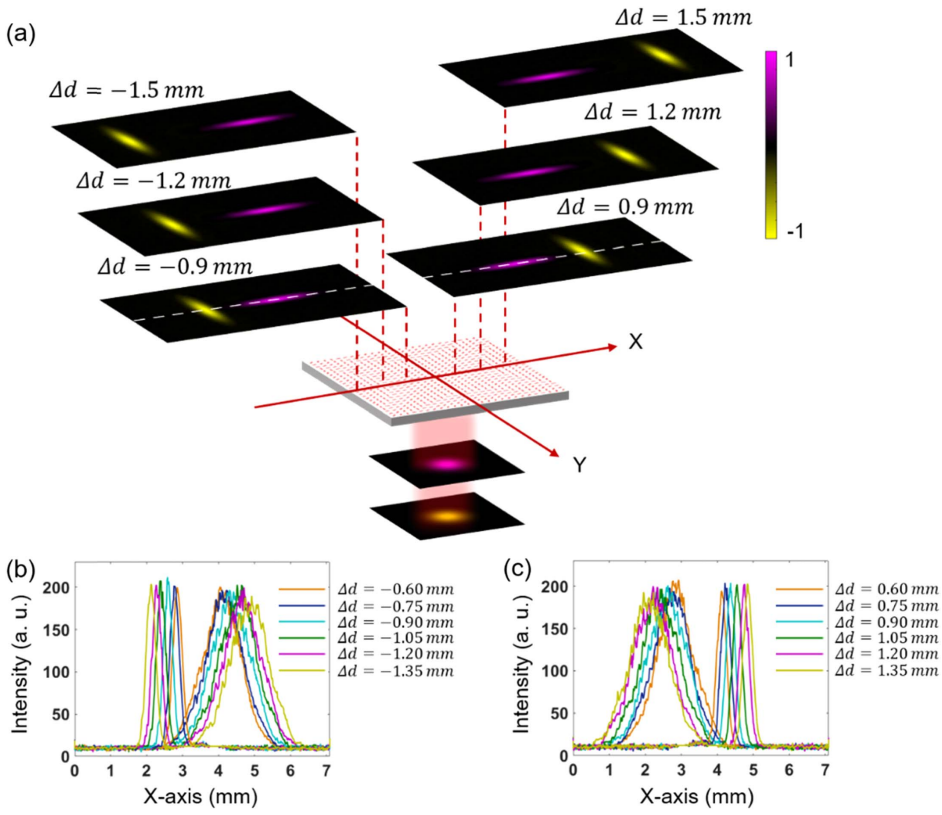

Fig. 4. (a) Measured Stokes parameters S_3 of the linearly polarized Gaussian beams at the incident position shifts of ±0.9, ±1.2, and ±1.5 mm. (b) and (c) Intensity curves corresponding to the white dashed lines across the intensity images at the incident position shifts of ±0.60, ±0.75, ±0.90, ±1.05, ±1.20, and ±1.35 mm.

shifts. For a quantitative comparison, we plot the intensity curves of the white dashed lines across the intensity images at the incident position shifts of ±0.60, ±0.75, ±0.90, ±1.05, ±1.20, and ±1.35 mm in Figs. 4(b) and 4(c). It is confirmed that the splitting of the two spin components depends on the magnitude of the incident position shift, and the locations of the LCP and RCP components depend on the sign of the incident position shift. The experimental results demonstrate that shifting the incident position on the metasurface is equivalent to imparting a gradient phase to the spin components of the output beam, which can produce SDS. We also measured the intervals between the LCP and RCP components with different incident position shifts, as shown in the blue circles in Fig. 5. According to Eq. (11), at the transmission distance of 500 mm, the intervals increase with the incident position shift and can be calculated as $|\rho| = 2.0159\Delta d$, denoted by the red line.

Owing to the P-B phase, the metasurface shows a dispersion-free characteristic in the visible region, which leads to a broadband working wavelength range. Figures 3(d)–3(f) show the results of the metasurface illuminated by a linearly polarized Gaussian beam with a shift of −1.2 mm at three different wavelengths (λ = 633, 532, and 475 nm). To obtain a better visual effect, we have done pseudocolor processing for the captured gray images, and the gray values [0, 255] are normalized as [0, 1]. From the diffraction patterns, the bright fringes maintain well. One of the significant parameters

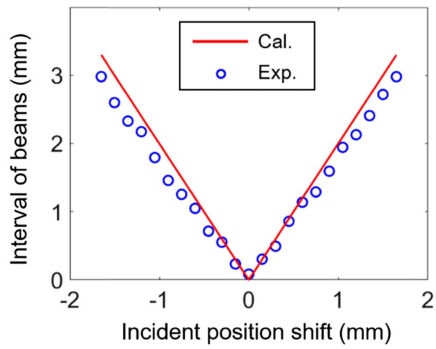

Fig. 5. Measured intervals between LCP and RCP components with different incident position shifts at the transmission distance of 500 mm. Cal., calculated; Exp., experimental.

to evaluate the performance of metasurface devices is the diffraction efficiency, defined as $\eta = (P_{LCP} + P_{RCP})/(P_{LCP} + P_{RCP} + P_0)$, where P_{LCP}, P_{RCP}, and P_0 are the output power of LCP, RCP, and zero-order components, respectively. The measured diffraction efficiencies approximate to 98.72%, 95.05%, and 90.06% at the wavelengths of 633, 532, and 475 nm. The corresponding transmission efficiencies (the ratio of the transmitted beam power and the incident beam power) are as high as 93.45%, 91.25%, and 88.54%.

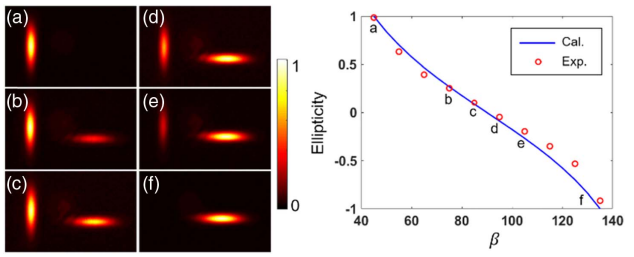

Fig. 6. Measured ellipticities versus the incident polarization (a function of β). (a)–(f) Optical intensity (normalized) profiles correspond to situations of $\beta = 45°, 75°, 85°, 95°, 105°$, and 135° at the wavelength of 633 nm. Cal., calculated; Exp., experimental.

2. Polarization Ellipticity Detection Based on SDS

Once the spin components of the incident beam are separated, the intensity ratio (τ) of the two components can be measured, which enables measuring the ellipticity [$\alpha = (1 - \sqrt{\tau})/(1 + \sqrt{\tau})$] and the handedness of polarized beams [20], where $\alpha = +1\,(-1)$ represents LCP (RCP), and $\alpha = 0$ represents linear polarization. Thus, the metasurface enables the polarization ellipticity detection of light by using the SDS. We test the polarization of Gaussian beams at the wavelength of 633 nm. The polarization state of the Gaussian beam is modulated by varying the angle (β) between the transmission axis of the polarizer and the fast axis of the quarter-wave plate (QWP). As shown in Fig. 6, the experimental results fit well with the theoretical predictions denoted by the blue curve, and we can obtain the theoretical predictions based on the Poincaré sphere theory. With the influence of zero order, there are slight differences between the theoretical values and the test results. However, the zero order can be suppressed by optimizing the design parameters of metasurface and processing technology. Thus, the metasurface can be used for the polarization ellipticity detection of polarized light.

B. Extra Phase Modulation of the Twisting Phase and Singular Beam Detection

Moreover, the extra phase modulation of the twisting phase is performed and successfully used for detecting singular beams. To verify this, a VB illuminates the metasurface with an incident position shift of −1.2 mm. Referring to the previous work [42], a polarizer, QWP, and conventional metasurface Q-plate ($q = 1$) are combined to generate circularly polarized VB with the topological charge of 2, which is transformed into linearly polarized VB with another QWP, as shown in part (i) of Fig. 7(a). The working mechanism of metasurface Q plate is similar to the fabricated metasurface, which modifies the birefringence of silica glass with the nanogrooves. The optical axis direction of the metasurface Q plate is designed as $\varphi = q\theta + \varphi_0$, where q is a certain constant, θ is the azimuthal angle, and φ_0 is the initial direction of the optical axis. The Stokes parameters S_3 of the output beam with different transmission distances ($z = 100$, 200, 300, 400, and 500 mm) are illustrated in Fig. 7(b). After passing through the metasurface, the VBs with LCP and RCP are separated, and the interval between them increases with the distance. Affected by the twisting phase, the intensity distributions of VBs diffract into several

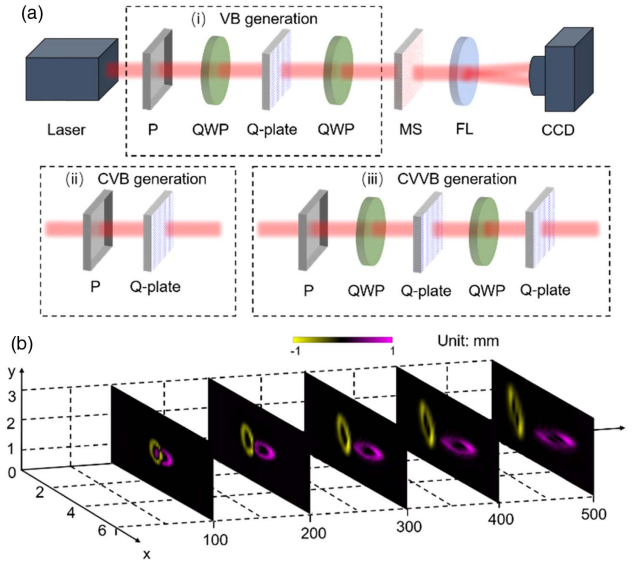

Fig. 7. (a) Schematic diagram of the experimental setups of arbitrarily singular beams detection based on the geometric P-B phase metasurface. P, polarizer; QWP, quarter-wave plate; MS, metasurface; FL, Fourier lens; CCD, charge-coupled device. (b) Measured S_3 parameters of the output beams with different transmission distances ($z = 100$, 200, 300, 400, and 500 mm).

bright and dark fringes, which is similar to the astigmatic transformation of VBs [43,44]. Because of the opposite twisting phases acting on the LCP and RCP components, there is a relative rotation between the diffraction patterns, which has no effect on the recognition of topological charge. By counting the number of dark fringes, the topological charges of the two sub-VBs can be obtained.

Because the beams with polarization singularities (CVB and CVVB) can be decomposed into two sub-VBs with orthogonal circular polarization states, the metasurface also enables detecting the polarization orders and topological charges of CVBs and CVVBs. According to our previous works [42,45], a single metasurface Q plate can be used to generate CVB with a linearly polarized Gaussian beam incident, and cascading two metasurface Q plates with a QWP can produce CVVBs, which are shown in parts (ii) and (iii) of Fig. 7(a). Then, the VBs (the topological charges are 1 and 2), CVBs (the polarization orders are −1 and 2), and CVVBs [the topological charges and polarization orders are (1, 2) and (2, −1)] are experimentally detected, which is illustrated in Fig. 8. The left columns show the theoretical phase and polarization profiles of singular beams. The far-field diffraction patterns are observed in the focal plane of the Fourier lens.

Regarding the vertical diffraction pattern and corresponding to the LCP VB, the direction of dark fringes is obliquely downward, indicating that the sign of topological charge is positive. On the contrary, the sign of topological charge is negative. In the horizontal diffraction pattern, the relationship is also valid, and we just need to rotate the diffraction pattern about 90° clockwise. Based on this relationship, the topological charges of LCP (l_L) and RCP (l_R) components from the VBs are (1, 1) and (2, 2), CVBs are (1, −1) and (−2, 2), and

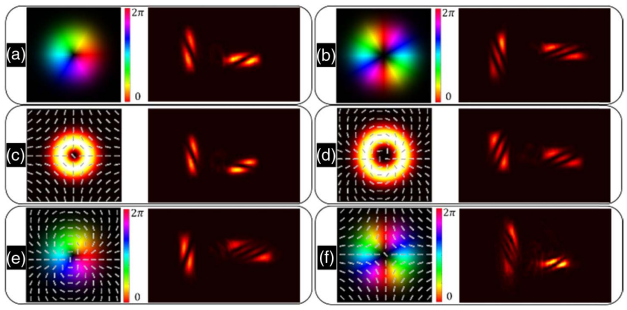

Fig. 8. (a) and (b) Experimental results of the VBs (the topological charges are 1 and 2) diffracting through the metasurface. (c) and (d) Experimental results of the CVBs (the polarization orders are −1 and 2) diffracting through the metasurface. (e) and (f) Experimental results of the CVVBs [the topological charges and polarization orders are (1, 2) and (2, −1)] diffracting through the metasurface. The gray lines represent the theoretical polarization profiles.

CVVBs are (−1, 3) and (3, 1). The topological charge (l) and polarization order (m) of these singular beams can be calculated by $l = (l_L + l_R)/2$, $m = (l_R - l_L)/2$. Finally, by substituting $(l_L + l_R)$ with (1, 1), (2, 2), (1, −1), (−2, 2), (−1, 3), and (3, 1), the calculated (l, m) of singular beams is (1, 0), (2, 0), (0, −1) (0, 2), (1, 2), and (2, −1), respectively.

4. DISCUSSION

Conventional tunable SDSs are realized via tailoring the structure of devices or the incident light beams, which are not good for integration systems. Except for the SDS, extra phase modulation functions are always pursued for performing more operations on the spin components, which is hard to meet with conventional methods. Tunable metasurfaces based on phase change and elastic materials are potential solutions because the characteristics of materials are thermally and mechanically tunable. It has also been demonstrated that a single metasurface can be used to perform multiple functions by integrating different functional phases. The chalcogenide phase change material composed of alloys of germanium, antimony, and tellurium can be transited between the disordered-amorphous state and ordered-crystalline state with temperature control, which is used for manipulating the "ON" and "OFF" state of the metasurface. However, the manipulation ability in the regulation range and continuous adjustability of these methods are quite limited because of the finite response states of materials. Hence, the controllable SHEs might come from a new tuning mechanism without involving tunable materials. Through mathematical deduction, we found that the phases with the functional structures of $a(x^2 - y^2)$, $a(x^2 + y^2)$, and axy adding together gradient phases are equivalent to performing a coordinate translation to original phases. To achieve controllable SHE, we just need to encode specific phases into the P-B phase devices. The proposed phase function construction method is free of the limitations of materials and shows a powerful ability in manipulating the regulation range, continuous adjustability, and stability. The twisting phase and the dynamical phase lens with the functional structures of $u(x^2 - y^2)$ and $\pi(x^2 + y^2)/\lambda f$ satisfy the conditions and can be used to manipulate the photonic SHE. It is found that the interval and the locations of the two separated spin components can be manipulated via shifting the incident beam with respect to the center of the P-B phase device, which provides a route for controllable SDS. With the action of the original phases, the extra phase modulation of the two spin components can also be achieved simultaneously. Except for the twisting phase and the dynamic phase lens, the other phases with similar functional structures are also expected for modulating beams and developing more interesting applications.

Meanwhile, owing to the dispersion-free characteristic originating from the geometric phase [21], the fabricated P-B phase metasurface is broadband in the visible region with high diffraction efficiency. After making full use of the SDS and the extra phase modulation of original phases, some interesting applications are raised. After passing through the metasurface, the two spin components of the incident beam are separated, and their intensity can be measured separately to detect the polarization ellipticity of light beams. Based on the relationship between the two separated spin components' interval and the incident position shift, a position sensor can also be constructed. Under the modulation of twisting phases, the metasurface also enables detecting the topological charges and polarization orders of arbitrary singular beams, which is a candidate mode demodulator in singular light modulation communication. Hence, the controllable SHE based on phase function construction might bring new opportunities for exploiting the spin and orbital angular momentum of light for optical information processing and communication. Moreover, the proposed controllable SHE scheme can be generalized to other physical systems because of the similar manipulation mechanism, such as electron beams [46].

5. CONCLUSION

In conclusion, we propose a controllable SHE mechanism based on phase function construction, which can be used for manipulating the SDS of light in the momentum space. Moreover, extra phase modulation of the two spin components during the SDS is achieved with the original phases. The twisting phase, which is achieved by engineering spatially variant nanogrooves in the fused silica glass substrate under the P-B phase mechanism, is selected to verify this mechanism. It is experimentally demonstrated that the tunable SDS can be realized by shifting the incident light onto the metasurface in the whole visible region with diffraction efficiency up to 98.72%, 95.05%, and 90.06% at the wavelengths of 633, 532, and 475 nm. The polarization ellipticity detection is also demonstrated with the help of the SDS effect. Furthermore, the extra phase modulation of the twisting phase is successfully used for detecting the topological charge and polarization order of singular beams. It is proved that the proposed controllable SHE based on phase function construction can be used not only for manipulating the photonic SDS but also other applications with the original phase modulation. This controllable SHE manipulation method provides a possible route for manipulating spin-polarized photons and is also promising for optical sensing and communication.

APPENDIX A: SAMPLE FABRICATION

The diameter of the metasurface substrate is 25 mm, with a thickness of 3 mm. The structure region of the metasurface is 4 mm × 4 mm, and $u = 10\ \text{mm}^{-2}$. The metasurface is fabricated by using a femtosecond laser working at 1030 nm wavelength (the repetition rate is about 500 kHz), and the spatially variant nanogrooves are written in a fused silica glass substrate. The laser is focused about 250 μm below the surface of the glass. The glass substrate is mounted on a three-axial translation stage system controlled by the SCA software (Altechna Ltd.). The designed patterns can be mapped into the substrate by controlling the translation stage system, and the induced form birefringence can be achieved by changing the writing parameters of the nanogrooves. The refractive indices of the glass substrates are modulated with the laser-irradiated intensity, leading to the birefringence in the isotropic glass. And the uniform glass sample (SiO_2) decomposes into the porous glass (SiO_{2-x}). The phase retardation of the metasurface is chosen as π at the wavelength of 633 nm, and the writing depth h is about 750 μm.

Funding. Program of Fundamental Research of Science and Technology Planning Project of Shenzhen Municipality (JCYJ20180507182035270); Science and Technology Planning Project of Guangdong Province (2016B050501005); Science and Technology Project of Shenzhen (ZDSYS201707271014468); International Collaborative Laboratory of 2D Materials for Optoelectronics Science and Technology (2DMOST2018003); National Natural Science Foundation of China (61805087, 61805149); Natural Science Foundation of Guangdong Province (2016A030310065, 2018A030313368, 2020A1515011392).

Disclosures. The authors declare no conflict of interest.

†These authors contributed equally to this work.

REFERENCES

1. K. Y. Bliokh and Y. P. Bliokh, "Conservation of angular momentum, transverse shift, and spin Hall effect in reflection and refraction of an electromagnetic wave packet," Phys. Rev. Lett. **96**, 073903 (2006).
2. K. Y. Bliokh, A. Niv, V. Kleiner, and E. Hasman, "Geometrodynamics of spinning light," Nat. Photonics **2**, 748–753 (2008).
3. M. Onoda, S. Murakami, and N. Nagaosa, "Hall effect of light," Phys. Rev. Lett. **93**, 083901 (2004).
4. T. Zhu, Y. Lou, Y. Zhou, J. Zhang, J. Huang, Y. Li, H. Luo, S. Wen, S. Zhu, and Q. Gong, "Generalized spatial differentiation from the spin Hall effect of light and its application in image processing of edge detection," Phys. Rev. Appl. **11**, 034043 (2019).
5. J. Zhou, H. Qian, C.-F. Chen, J. Zhao, G. Li, Q. Wu, H. Luo, S. Wen, and Z. Liu, "Optical edge detection based on high-efficiency dielectric metasurface," Proc. Natl. Acad. Sci. USA **116**, 11137–11140 (2019).
6. X. Zhou, Z. Xiao, H. Luo, and S. Wen, "Experimental observation of the spin Hall effect of light on a nanometal film via weak measurements," Phys. Rev. A **85**, 043809 (2012).
7. X. Zhou, X. Ling, H. Luo, and S. Wen, "Identifying graphene layers via spin Hall effect of light," Appl. Phys. Lett. **101**, 251602 (2012).
8. O. Hosten and P. Kwiat, "Observation of the spin Hall effect of light via weak measurements," Science **319**, 787–790 (2008).
9. X. Zhou, L. Sheng, and X. Ling, "Photonic spin Hall effect enabled refractive index sensor using weak measurements," Sci. Rep. **8**, 1221 (2018).
10. K. Y. Bliokh, Y. Gorodetski, V. Kleiner, and E. Hasman, "Coriolis effect in optics: unified geometric phase and spin-Hall effect," Phys. Rev. Lett. **101**, 030404 (2008).
11. Y. Qin, Y. Li, H. He, and Q. Gong, "Measurement of spin Hall effect of reflected light," Opt. Lett. **34**, 2551–2553 (2009).
12. X. Ling, X. Zhou, K. Huang, Y. Liu, C.-W. Qiu, H. Luo, and S. Wen, "Recent advances in the spin Hall effect of light," Rep. Prog. Phys. **80**, 066401 (2017).
13. Z. E. Bomzon, V. Kleiner, and E. Hasman, "Pancharatnam–Berry phase in space-variant polarization-state manipulations with subwavelength gratings," Opt. Lett. **26**, 1424–1426 (2001).
14. J. Ren, Y. Li, Y. Lin, Y. Qin, R. Wu, J. Yang, Y.-F. Xiao, H. Yang, and Q. Gong, "Spin Hall effect of light reflected from a magnetic thin film," Appl. Phys. Lett. **101**, 171103 (2012).
15. L. Marrucci, C. Manzo, and D. Paparo, "Optical spin-to-orbital angular momentum conversion in inhomogeneous anisotropic media," Phys. Rev. Lett. **96**, 163905 (2006).
16. D. Haefner, S. Sukhov, and A. Dogariu, "Spin Hall effect of light in spherical geometry," Phys. Rev. Lett. **102**, 123903 (2009).
17. X. Zhou, X. Ling, Z. Zhang, H. Luo, and S. Wen, "Observation of spin Hall effect in photon tunneling via weak measurements," Sci. Rep. **4**, 7388 (2014).
18. K. Y. Bliokh, C. T. Samlan, C. Prajapati, G. Puentes, N. K. Viswanathan, and F. Nori, "Spin-Hall effect and circular birefringence of a uniaxial crystal plate," Optica **3**, 1039–1047 (2016).
19. O. Takayama and G. Puentes, "Enhanced spin Hall effect of light by transmission in a polymer," Opt. Lett. **43**, 1343–1346 (2018).
20. D. Wen, F. Yue, S. Kumar, Y. Ma, M. Chen, X. Ren, P. E. Kremer, B. D. Gerardot, M. R. Taghizadeh, G. S. Buller, and X. Chen, "Metasurface for characterization of the polarization state of light," Opt. Express **23**, 10272–10281 (2015).
21. J. Zhou, H. Qian, G. Hu, H. Luo, S. Wen, and Z. Liu, "Broadband photonic spin Hall meta-lens," ACS Nano **12**, 82–88 (2017).
22. S. Chen, Y. Cai, G. Li, S. Zhang, and K. W. Cheah, "Geometric metasurface fork gratings for vortex-beam generation and manipulation," Laser Photon. Rev. **10**, 322–326 (2016).
23. X. Bai, L. Tang, W. Lu, X. Wei, S. Liu, Y. Liu, X. Sun, H. Shi, and Y. Lu, "Tunable spin Hall effect of light with graphene at a telecommunication wavelength," Opt. Lett. **42**, 4087–4090 (2017).
24. X. Ling, X. Zhou, W. Shu, H. Luo, and S. Wen, "Realization of tunable photonic spin Hall effect by tailoring the Pancharatnam–Berry phase," Sci. Rep. **4**, 5557 (2014).
25. A. E. Minovich, A. E. Miroshnichenko, A. Y. Bykov, T. V. Murzina, D. N. Neshev, and Y. S. Kivshar, "Functional and nonlinear optical metasurfaces," Laser Photon. Rev. **9**, 195–213 (2015).
26. Q. He, S. Sun, S. Xiao, and L. Zhou, "High-efficiency metasurfaces: principles, realizations, and applications," Adv. Opt. Mater. **6**, 1800415 (2018).
27. L. Zhang, S. Mei, K. Huang, and C.-W. Qiu, "Advances in full control of electromagnetic waves with metasurfaces," Adv. Opt. Mater. **4**, 818–833 (2016).
28. X. Luo, M. Pu, X. Li, and X. Ma, "Broadband spin Hall effect of light in single nanoapertures," Light: Sci. Appl. **6**, e16276 (2017).
29. A. P. Slobozhanyuk, A. N. Poddubny, I. S. Sinev, A. K. Samusev, Y. F. Yu, A. I. Kuznetsov, A. E. Miroshnichenko, and Y. S. Kivshar, "Enhanced photonic spin Hall effect with subwavelength topological edge states," Laser Photon. Rev. **10**, 656–664 (2016).
30. Y. Liu, Y. Ke, H. Luo, and S. Wen, "Photonic spin Hall effect in metasurfaces: a brief review," Nanophotonics **6**, 51–70 (2017).
31. O. Takayama, J. Sukham, R. Malureanu, A. V. Lavrinenko, and G. Puentes, "Photonic spin Hall effect in hyperbolic metamaterials at visible wavelengths," Opt. Lett. **43**, 4602–4605 (2018),
32. X. Ling, X. Zhou, X. Yi, W. Shu, Y. Liu, S. Chen, H. Luo, S. Wen, and D. Fan, "Giant photonic spin Hall effect in momentum space in a structured metamaterial with spatially varying birefringence," Light: Sci. Appl. **4**, e290 (2015).

33. Y. Li, Y. Liu, X. Ling, X. Yi, X. Zhou, Y. Ke, H. Luo, S. Wen, and D. Fan, "Observation of photonic spin Hall effect with phase singularity at dielectric metasurfaces," Opt. Express **23**, 1767–1774 (2015).
34. X. Yin, Z. Ye, J. Rho, Y. Wang, and X. Zhang, "Photonic spin Hall effect at metasurfaces," Science **339**, 1405–1407 (2013).
35. W. Luo, S. Xiao, Q. He, S. Sun, and L. Zhou, "Photonic spin Hall effect with nearly 100% efficiency," Adv. Opt. Mater. **3**, 1102–1108 (2015).
36. X. Yin, T. Steinle, L. Huang, T. Taubner, M. Wuttig, T. Zentgraf, and H. Giessen, "Beam switching and bifocal zoom lensing using active plasmonic metasurfaces," Light: Sci. Appl. **6**, e17016 (2017).
37. S. M. Kamali, E. Arbabi, A. Arbabi, Y. Horie, and A. Faraon, "Highly tunable elastic dielectric metasurface lenses," Laser Photon. Rev. **10**, 1002–1008 (2016).
38. M. Zhang, M. Pu, F. Zhang, Y. Guo, Q. He, X. Ma, Y. Huang, X. Li, H. Yu, and X. Luo, "Plasmonic metasurfaces for switchable photonic spin-orbit interactions based on phase change materials," Adv. Sci. **5**, 1800835 (2018).
39. D. Shen and D. Zhao, "Measuring the topological charge of optical vortices with a twisting phase," Opt. Lett. **44**, 2334–2337 (2019).
40. R. Drevinskas and P. G. Kazansky, "High-performance geometric phase elements in silica glass," APL Photon. **2**, 066104 (2017).
41. S. Chen, X. Zhou, Y. Liu, X. Ling, H. Luo, and S. Wen, "Generation of arbitrary cylindrical vector beams on the higher order Poincaré sphere," Opt. Lett. **39**, 5274–5276 (2014).
42. Y. He, Y. Li, J. Liu, X. Zhang, Y. Cai, Y. Chen, S. Chen, and D. Fan, "Switchable phase and polarization singular beams generation using dielectric metasurfaces," Sci. Rep. **7**, 6814 (2017).
43. V. Denisenko, V. Shvedov, A. S. Desyatnikov, D. N. Neshev, W. Krolikowski, A. Volyar, M. Soskin, and Y. S. Kivshar, "Determination of topological charges of polychromatic optical vortices," Opt. Express **17**, 23374–23379 (2009).
44. A. Y. Bekshaev and A. I. Karamoch, "Astigmatic telescopic transformation of a high-order optical vortex," Opt. Commun. **281**, 5687–5696 (2008).
45. Y. He, P. Wang, C. Wang, J. Liu, H. Ye, X. Zhou, Y. Li, S. Chen, X. Zhang, and D. Fan, "All-optical signal processing in structured light multiplexing with dielectric meta-optics," ACS Photon. **7**, 135–146 (2020).
46. E. Karimi, L. Marrucci, V. Grillo, and E. Santamato, "Spin-to-orbital angular momentum conversion and spin-polarization filtering in electron beams," Phys. Rev. Lett. **108**, 044801 (2012).